JOURNAL OF SOLID STATE CHEMISTRY **141,** 121–132 (1998)
ARTICLE NO. SC987927

Crystal Chemistry and Phase Transitions of Perovskite in *P–T–X* Space: Data for $(K_xNa_{1-x})MgF_3$ Perovskites

Yusheng Zhao

LANSCE, MS-H805, Los Alamos National Laboratory, Los Alamos, New Mexico 87545

Received January 22, 1998; in revised form June 8, 1998; accepted June 9, 1998

We report a high-resolution synchrotron X-ray powder diffraction study on $(K_xNa_{1-x})MgF_3$ perovskites at high pressures and temperatures. The crystal structure of the perovskite transforms reversibly from orthorhombic (*Pbnm*) to tetragonal (*P*4/*mbm*) to cubic (*Pm*3*m*) with change of pressure and temperature and also with K^+ concentration. The tilt angle of the MgF_6 octahedral framework decreases continually and the octahedral Mg–F bond length increases slightly with increasing temperature. Correspondingly, at high pressures, the tilting angles increase slightly and the shortening of the Mg–F bond length is the dominant compression mechanism. Both octahedral tilting and bond length decrease with increasing K^+ participation. We have monitored superlattice diffraction associated with in-phase and antiphase octahedral tiltings *in situ* and in real time in *P–T–X* space. The intensities of the superlattice diffraction peaks decrease quickly toward zero with increasing temperature and/or K^+ concentration. Meanwhile, the doublet and triplet diffraction peaks, which directly reflect the dimensional differences of the *a*, *b*, and *c* axes, converge continuously and finally coalesce into single peaks as the temperature reaches T_c and/or the K^+ concentration reaches X_c. The transition temperatures are plotted as a function of pressure (T_c–*P*), and as a function of composition (T_c–*X*). The structural phase transitions in $(K,Na)MgF_3$ perovskites are driven by two order parameters, which are represented by the octahedral tiltings $\theta=(\phi_x^-, \phi_y^-, 0)$ and $\varphi=(0, 0, \phi_z^+)$. The strong coupling between these two order parameters drives the end-member $NaMgF_3$ perovskite to transform directly from the orthorhombic to cubic phase at temperature $T_c=1038$ K. Such direct orthorhombic–cubic phase transition remains unbroken even at pressures up to 10 GPa. However, with increasing incorporation of larger K^+ cations into the crystal structure, the interaction between the octahedral tiltings was successively decoupled and the purely intermediate tetragonal phase thus appeared around $X \sim 35\%$. The crystal structure of the $(K_xNa_{1-x})MgF_3$ perovskites eventually becomes cubic at $X \sim 40\%$.

INTRODUCTION

Materials with the perovskite structure, or topologically closely related structures, have been of great interest to the condensed matter physics, solid state chemistry, and materials science communities over past four decades. Perovskites are well known for manifesting different types of structural distortions and accommodating a large variety of chemical compositions and also for having significant changes in physical properties and displaying critical phenomena during structural phase transitions. They find many technological applications today in ceramics, refractories, electronics, and high-T_c superconductors. Research on perovskite structures has been extended to $(Mg,Fe)SiO_3$ silicates to study density, melts, rheology, and thermoelasticity at extremely high pressures and temperatures to infer the composition and dynamics of the Earth's deep mantle.

The perovskite structure is a corner-linked octahedral framework and can be readily distorted from its cubic prototype by changes of pressure (P), temperature (T), and chemical composition (X). The most common distorted perovskites are characterized either by cation shifts or by octahedral tilts. The centrosymmetrically distorted orthorhombic perovskites with space group *Pbnm* (D_{2h}^{16}) are distorted by two independent octahedral tiltings θ and φ, where θ is an antiphase tilt about the pseudocubic $\langle 110\rangle_p$ axes, $\theta = (\phi_x^-, \phi_y^-, 0)$, and φ is an in-phase tilt about the pseudocubic $\langle 001\rangle_p$ axis of the octahedra, $\varphi = (0, 0, \phi_z^+)$ (Fig. 1). It can also be demonstrated that, geometrically, these two tilts can be represented by only one tilt, $\Phi = (\phi_x^-, \phi_y^-, \phi_z^+)$, about the $\langle 111\rangle_p$ axis of the regular octahedra (1, 2). The orthorhombic *Pbnm* phase of perovskite is also denoted $(a^-a^-c^+)$ in *Glazer's* scheme (3, 4). The nature of these octahedral tilts is directly associated with the vibrational instability of the crystal lattice. Particular zone-boundary phonon modes M_3 and R_{25} undergo critical softening and condensation processes as pressure and temperature changes (5–7). The freeze-in static part of the atomic displacements will thus lead to in-phase tilting ϕ^+ and antiphase tilting ϕ^-, respectively (Fig. 2a). Combinations of in-phase tilting ϕ^+ and antiphase tilting ϕ^- will then generate distinct space groups with different classes of superlattice diffractions. The observation of particular superlattice reflections can thus be used as a diagnostic

0022-4596/98 $25.00

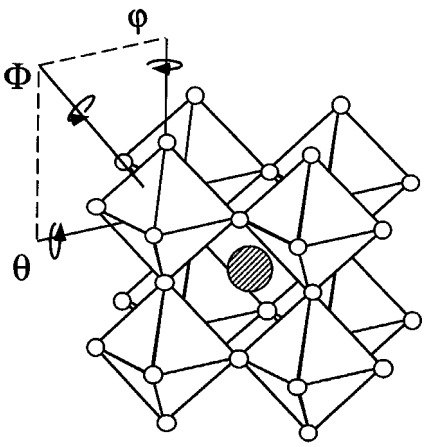

FIG. 1. Octahedral framework of an ideal cubic *Pm3m* perovskite. The centrosymmetrically distorted orthorhombic perovskite with a space group of *Pbnm* is derived through the combination of the octahedral rotation φ about $\langle 001\rangle_{pc}$ and the octahedral tilting θ about $\langle 110\rangle_{pc}$. It can also be conceived as the result of tilting Φ about the threefold $\langle 111\rangle_{pc}$ axes of the regular octahedra.

indication for specific structural phases of the perovskite associated with a particular tilting system (Fig. 2b).

The present work is a continuation of a comprehensive study of fluoride perovskite (11, 12, 20–22, 29). We have studied the change of lattice parameters, tilting angles, octahedral bond lengths, and thermal vibration as functions of pressure (P), temperature (T), and chemical composition (X). The superlattice diffractions and critical phenomena associated with phase transitions of the perovskite structure are monitored in P–T–X space. A structural model is proposed to interpret the compression and thermal expansion of the perovskite lattice from the point of view of octahedral tilting and bond length.

EXPERIMENTAL

A. Composition Effects

$(K_xNa_{1-x})MgF_3$ perovskites were synthesized with stoichiometric proportions of KF, NaF, and MgF_2 at 1073 K for 8 h in a sealed alumina crucible. The K^+ molar

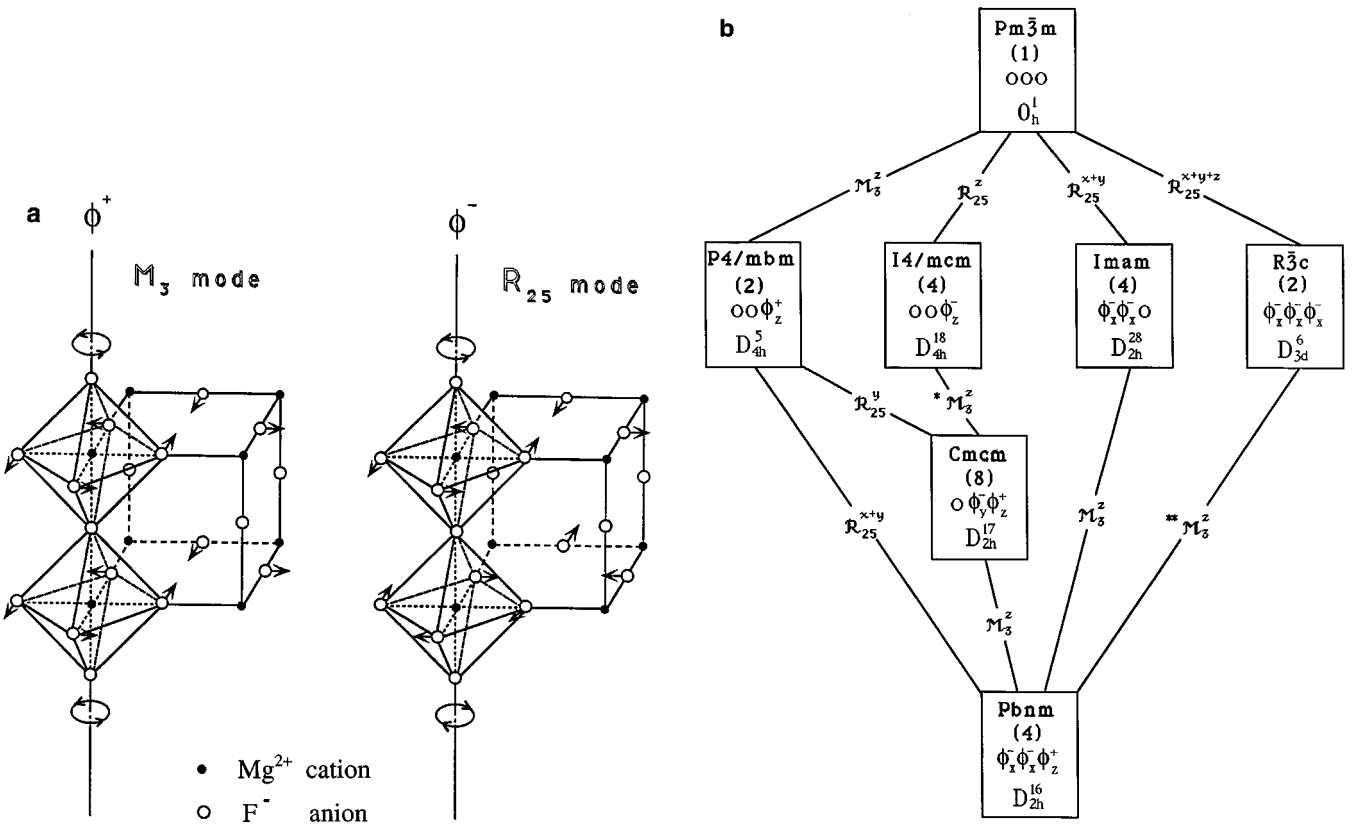

FIG. 2. (a) The in-phase tilting ϕ^+, due to condensation of the M_3 soft mode, denotes the *same* sense of rotation for successive octahedral layers, while the anti-phase tilting ϕ^-, due to condensation of the R_{25} soft mode, denotes the *opposite* sense of rotation for successive octahedral layers. (b) Probable sequences ("routes") of the successive structural phase transitions from the *Pbnm* orthorhombic phase up to the *Pm3m* cubic phase in perovskites. M_3 and R_{25} are soft modes with reference to the cubic Brillouin zone and are believed to be the driving mechanisms of the corresponding phase transitions. The tilting ϕ about the given tilting axis (with reference to prototype cubic cell) is denoted by the subscript of $\phi_{(xyz)}$. The diagram is drawn after Aleksandrov (5).

concentration was controlled to a $\Delta X = 5\%$ step and over the range $X = 0$–50% for $(K_xNa_{1-x})MgF_3$. High-resolution synchrotron X-ray powder diffraction data were collected in the angle-dispersive mode (8) using a position-sensitive detector (PSD) at the X7A beamline of NSLS, Brookhaven. The data were collected at 2θ Bragg angles up to 60° with a monochromatic wavelength of $\lambda = 0.6992$ Å and were analyzed with the *Rietveld* refinement method (9) using GSAS (10). By least-squares minimizing the difference between the observed diffraction pattern and a synthetic model pattern, one can refine the unit cell dimensions, atomic positions, and thermal vibrations of the crystal structure simultaneously. Diffraction spectra of $(K_xNa_{1-x})MgF_3$ perovskites for various values of x, stacked in a diagram (Fig. 3), show that the orthorhombic perovskite structure becomes less distorted as more larger K^+ cations replace smaller Na^+ cations. This is revealed in the diffraction spectra as the intensities of the orthorhombic superlattice diffraction peaks gradually decrease and the peak splittings of the doublets and triplets continually coalesce, eventually producing single peaks. The convergence of the *a*, *b*, and *c* axes with increasing K^+ content is a clear indication of the decrease of structural distortion and the development of phase transitions (Fig. 4). By monitoring the appearance and disappearance of the superlattice diffraction peaks, we have positively identified the existence of the pure tetragonal phase in the $X = 30$–40% range. Above $X = 0.4$, the $(K_xNa_{1-x})MgF_3$ perovskites become cubic.

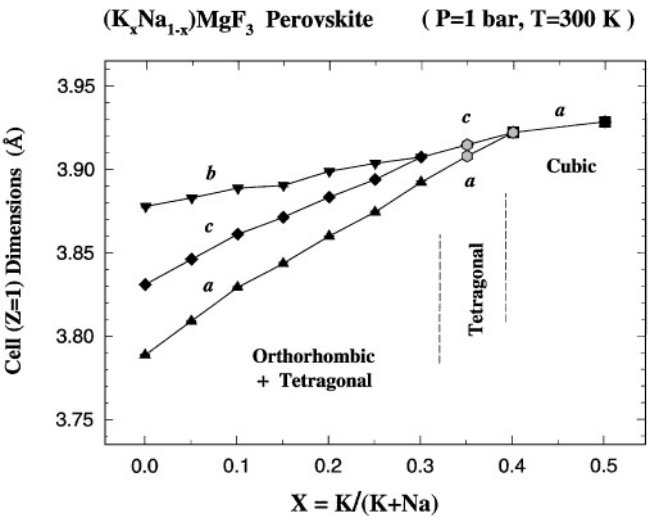

FIG. 4. Unit cell parameters (reduced to a pseudocubic $Z = 1$ prototype cell) of $(K_xNa_{1-x})MgF_3$ perovskite as a function of K^+ concentration. The unit cell dimensions increase and converge accompanied with two structural phase transitions for the perovskite structure as $X = K/(K + Na)$ increases.

The orthorhombic *Pbnm* phase of $(K_xNa_{1-x})MgF_3$ perovskite becomes less distorted with increasing concentration of K^+ cations. All three tilts in the $(\phi_x^-, \phi_y^-, \phi_z^+)$ system of the orthorhombic structure diminish gradually as X increases. The antiphase tilting $\theta = (\phi_x^-, \phi_y^-, 0)$ of the MgF_6

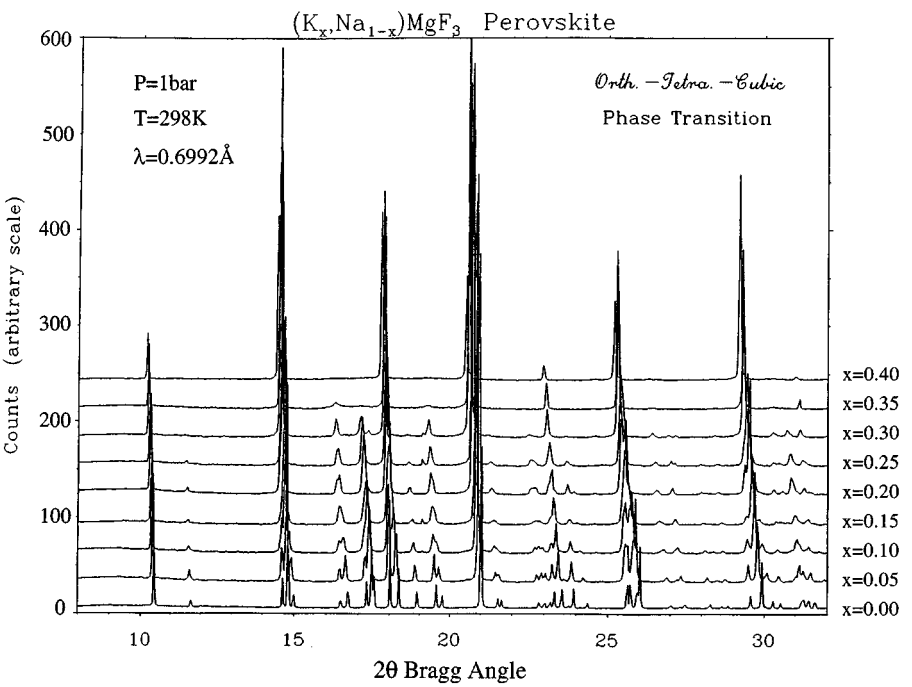

FIG. 3. Powder X-ray diffraction pattern of $(K_xNa_{1-x})MgF_3$ perovskites stacked for $X = 0.0$ to $X = 0.4$ with $\Delta X = 0.05$ steps. For structural refinement, the actual experimental data were collected up to $2\theta = 60°$.

octahedra decreases drastically and eventually becomes zero as the concentration of K^+ increases up to $X \sim 35\%$ (Fig. 5). The perovskite structure becomes purely tetragonal $P4/mbm$ (D_{4h}^5). The in-phase tilting $\varphi = (0, 0, \phi_z^+)$ also decreases as more K^+ cations are incorporated into the perovskite structure and it eventually becomes zero at $X \sim 40\%$ and results in the cubic phase. With increasing concentration of the large K^+ cations, the octahedral Mg–F bond length is essentially constant for the first 0–25% of K^+ concentration (Fig. 6). However, the Mg–F bond drastically shrinks as the crystal structure of the $(K,Na)MgF_3$ perovskite approaches the tetragonal and cubic phases. The convergence of the lattice parameters, drastic shrinkage of the octahedral bond length, and rapid decreases of octahedral tiltings around the transition composition X_c are very similar to the critical softening phenomena observed around the transition temperature T_c for the end-member $NaMgF_3$ perovskite (11, 12). A major observation of the composition effects in the present study is the existence of a secondary phase with the main phase, which is discussed in a later section.

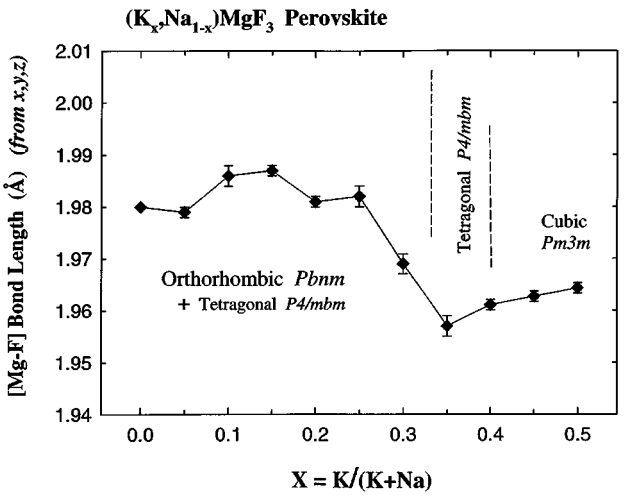

FIG. 6. Mean Mg–F bond length derived from positional parameters x, y, z plotted as a function of K^+ concentration for $(K_xNa_{1-x})MgF_3$ perovskites. Notice the drastic shortening of the Mg–F bond length as structural phase transitions occur.

B. Temperature Effects

We heated the $(K,Na)MgF_3$ perovskite samples to high temperatures and monitored the appearance of superlattice diffraction peaks and peak splitting with the position-sensitive detector. The PSD simultaneously observes a section of diffraction pattern 12° wide in 2θ Bragg angle. It can thus monitor the structural phase transition *in situ* and in real time at high temperatures. A selected section of the diffraction pattern for the $(K_{0.15}Na_{0.85})MgF_3$ perovskites is plotted for elevated temperatures in Fig. 7. The structural phase transition from orthorhombic *Pbnm* to tetragonal *P*4/*mbm* is clearly shown by the disappearance of superlattice peaks $\{121, 103, 211\}_{orth}$ and $(113)_{orth}$ and also by the coalescence of the doublet peaks $\{022, 202\}_{orth}$ at T_{c1}(orth–tetra) ≈ 673 K (see Fig. 14 for the peak indexing), whereas the structural phase transition from tetragonal *P*4/*mbm* to cubic *Pm3m* is evidently shown by the disappearance of superlattice peaks $(210)_{tetra}$ and $(211)_{tetra}$ at T_{c2}(tetra–cubic) ≈ 923 K. The T_c–X phase diagram for the orthorhombic, tetragonal, and cubic phases is thus mapped out for the $(K_xNa_{1-x})MgF_3$ perovskites as shown in Fig. 8. These observations are further confirmed by whole pattern refinement using the Rietveld method.

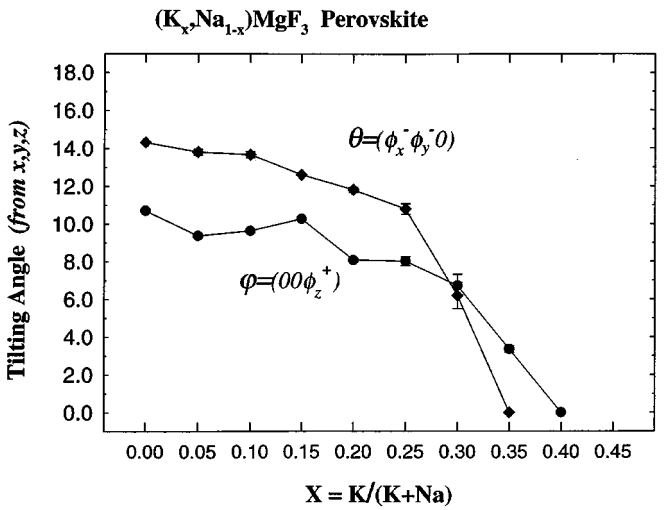

FIG. 5. Octahedral tiltings θ and φ from positional parameters x, y, z plotted as a function of K^+ concentration for $(K_xNa_{1-x})MgF_3$ perovskites. Notice the significant diminishing of octahedral tiltings as structural phase transitions occur.

There are three interesting features in this phase diagram: First, the strong coupling between two order parameters for the end-member $NaMgF_3$ (11, 12) has been broken down (see discussions in the next paragraph) as a result of incorporation of the large K^+ cations into the perovskite structure. The intermediate tetragonal phase *P*4/*mbm* can now be observed at elevated temperature. Second, the transition temperature T_c decreases as the K^+ concentration increases. The tetragonal and cubic phases of the $(K_xNa_{1-x})MgF_3$ perovskites can be stable even at ambient conditions. Third, there exists a kink on the phase boundary between orthorhombic *Pbnm* and tetragonal *P*4/*mbm* at about $X = 15\%$, which is associated with abnormal (out of trend) refinement results on lattice parameters, octahedral tilts, and bond lengths around 15% K^+ concentration (Figs. 4–6). When looking more closely into the details of diffraction spectra and also the results of Rietveld refinement of the orthorhombic structure for the $(K_xNa_{1-x})MgF_3$ perovskites, we find that the intensity of some major

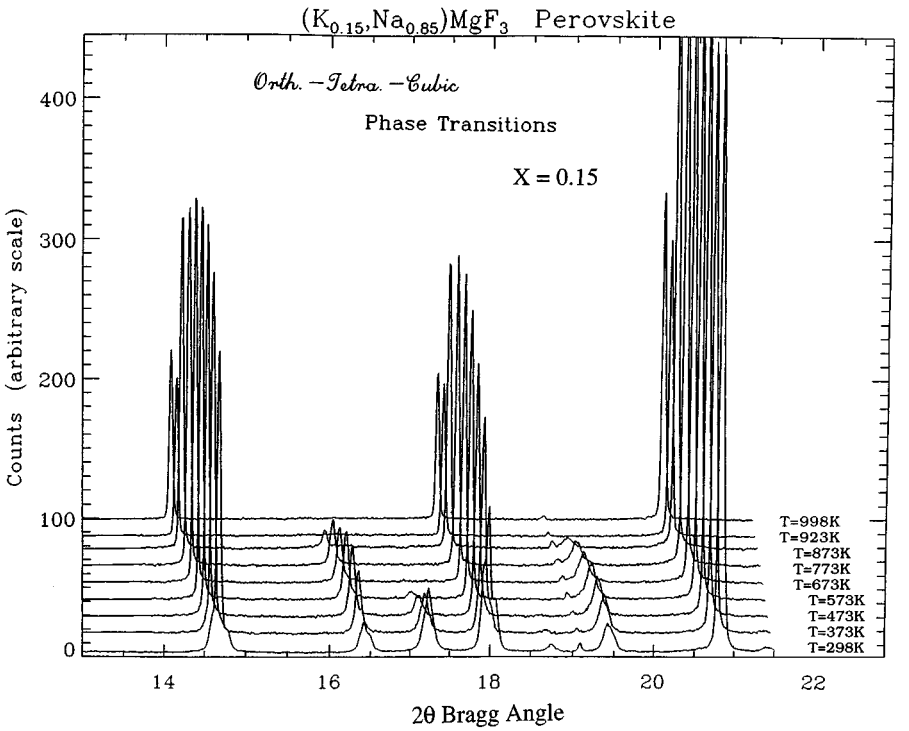

FIG. 7. Selected section of powder X-ray diffraction pattern (2θ range 13–23°) of $(K_xNa_{1-x})MgF_3$ perovskites monitored *in situ* and in real time during the high-T experiments. Notice the disappearance of superlattice diffraction peaks as the orthorhombic–tetragonal and the tetragonal–cubic phase transitions occur.

diffraction peaks cannot be fitted well enough and the diffraction spectrum cannot be index as the pure orthorhombic *Pbnm* phase. There are extra diffraction peaks related to in-phase tilting ϕ_z^+ of the octahedra that do not belong to the orthorhombic phase. It is suggested that a secondary phase must exist in the 10–30% K^+ concentration range (see later discussion).

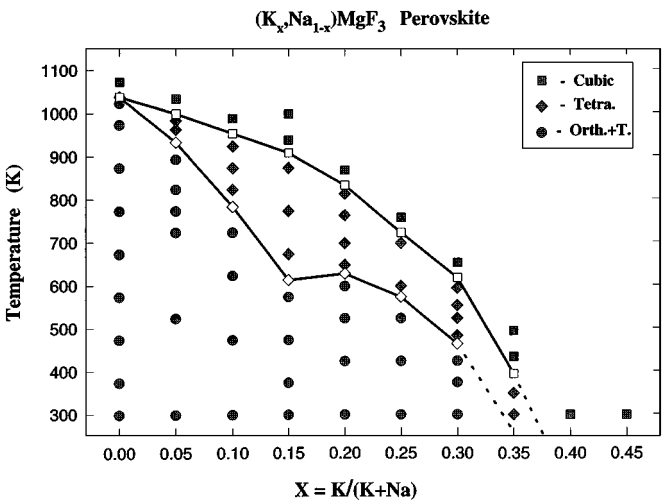

FIG. 8. T_c–X phase diagram showing the phase boundaries between orthorhombic *Pbnm*, tetragonal *P4/mbm*, and cubic *Pm3m*. The filled symbols are structural refinement results and the empty symbols with boundary lines are determined by *in situ* and real time monitoring during the experiment.

For the end-member $NaMgF_3$ perovskite, all of the octahedral tilts and structural distortion vanish at about the same temperature and the crystal structure virtually transforms from the orthorhombic *Pbnm* phase directly to the cubic *Pm3m* phase at $T_c = 1038$ K with no intermediate tetragonal phase (11, 12, 29). The tilt angles of the octahedral framework decrease with increasing temperature. As the temperature approaches the orthorhombic–cubic transition temperature(T_c), both tilts θ and φ decrease rapidly toward zero (Fig. 9) in a manner expected for a Landau-type ferroelastic phase transition (13). The octahedral Mg–F bond lengths first increase slowly with temperature and then shrink dramatically throughout a temperature interval of about 100 K prior to the transition (Fig. 10). The amplitude of the thermal vibration of the fluorine anions (F^-), refined as isotropic temperature factors, increases dramatically as the temperature approaches T_c. The anisotropic thermal vibration for F^- anions changes from an ellipsoidal shape in the orthorhombic *Pbnm* phase to a flat disk shape in the cubic *Pm3m* phase (see Figs. 7 and 8 in Ref. 11). The increase in the lateral/anharmonic thermal vibration of the octahedral framework leads to a strong interaction of the two independent vibrational modes R_{25} and M_3. It is

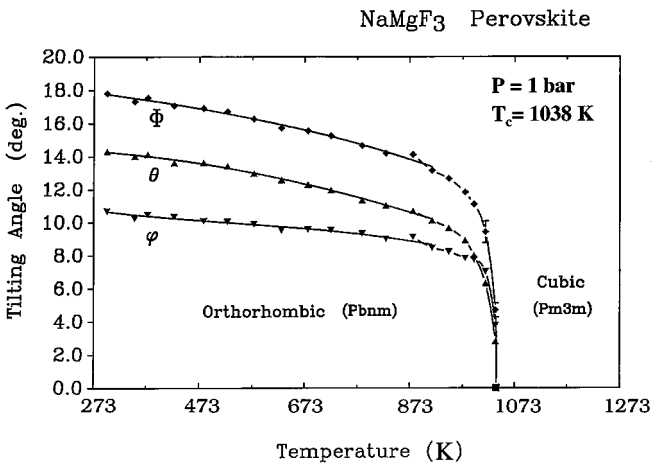

FIG. 9. Octahedral tiltings θ and φ derived from positional parameters x, y, z plotted as a function of temperature for the end-member $NaMgF_3$ perovskite. Notice that both tilts approach zero simultaneously, indicating the strong coupling of the two order parameters during the structural phase transition.

understood that these two tilts, θ and φ, are the direct results of the soft phonon modes R_{25} and M_3. Thus, the direct transformation of the crystal structure from the orthorhombic *Pbnm* phase to the cubic *Pm*3*m* phase is a result of significant coupling of the two order parameters θ and φ. The softening of phonon modes at the zone corner R and zone edge M points causes the fold-in of the Brillouin zone and results in distortion, multiplication, and reorientation of the crystal lattice (14, 15). From the point of view of lattice dynamics, the direct orthorhombic–cubic phase transition reflects the unfreezing or softening of the entire Brillouin

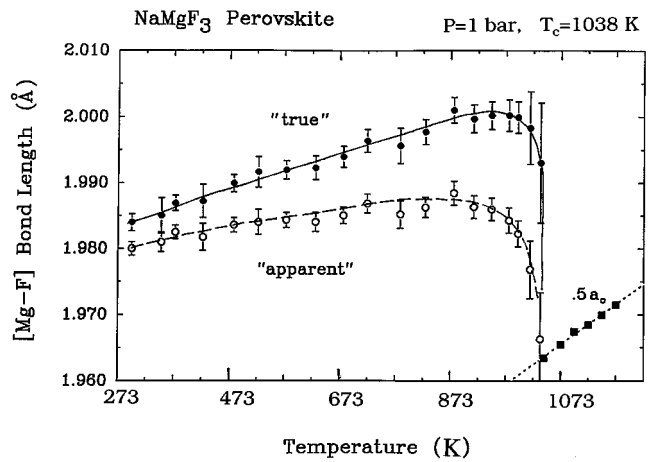

FIG. 10. Mean Mg–F bond length derived from positional parameters x, y, z plotted as a function of temperature for the end-member $NaMgF_3$ perovskite. Notice the drastic shortening of the Mg–F bond length as the structural phase transitions occur. The "true" bond length accounts for the contribution from the thermal vibration (ellipsoidal) effects.

branch from the R point to the M point at the transition temperature. We have also observed experimentally that thermal expansion and heat capacity (see Fig. 15 in Ref. 12 and Fig. 1 in Ref. 29), both of which are second derivatives of the free energy, show the typical λ shape around the transition temperature (12, 29). The critical phenomena associated with the structural phase transition observed for the $NaMgF_3$ perovskite can be well described by Landau theory. We know that it is the shape of the free energy surface that defines all of the structural and physical properties of the crystal. The multiminimum energy well in the orthorhombically distorted phase (Fig. 11) transforms into a single-minimum well in the cubic phase. It has a gentle and wide flat bottom at the transition temperature. The restoring force in the crystal lattice thus relaxes and the phonon constrained in the energy minimums becomes soft. As the orthorhombically displaced atoms unfreeze and move toward the single-minimum cubic position, many critical softening phenomena ("anomalies") for various physical properties are thus introduced, as observed in the optical phonons, thermal ellipsoids, thermal expansivity, and heat capacity (16, 17).

C. *Pressure Effects*

Pressure plays a role opposite to that of temperature in the centrosymmetrically distorted perovskite (18). With increasing pressure, the energy minimums in the orthorhombic phase become deeper and steeper and the perovskite structure becomes more distorted. We have conducted a high-pressure experiment on the $NaMgF_3$ perovskite using a large-volume multianvil press (SAM-85), installed at the X17B beamline of NSLS, Brookhaven. In an *in situ* high P–T synchrotron X-ray powder diffraction experiment, the whole diffraction pattern in the energy-dispersive mode can be viewed in real time by a solid state detector linked with a multichannel analyzer (19). We can monitor the superlattice peaks and thus phase transition, as pressure and temperature change. The orthorhombic–cubic phase transition is found to be reversible either by cooling or by increasing the pressure (20). There is no intermediate tetragonal phase observable within a temperature step of $\Delta T = 30$–50 K around the phase transition at high pressures. The orthorhombic–cubic phase boundary of the end-member $NaMgF_3$ perovskite, plotted in a T_c–P phase diagram (Fig. 12), is determined to have a positive slope of about 45 K/GPa, which is similar to what is observed for many other centrosymmetric perovskites.

The a, b, and c axes of the crystal lattice contract and diverge smoothly as pressure increases. Upon heating, the a, b, and c axes expand and converge continually and eventually become identical in the cubic phase. These observations suggest that the structural distortion of the perovskite increases with pressure and decreases with temperature. It is

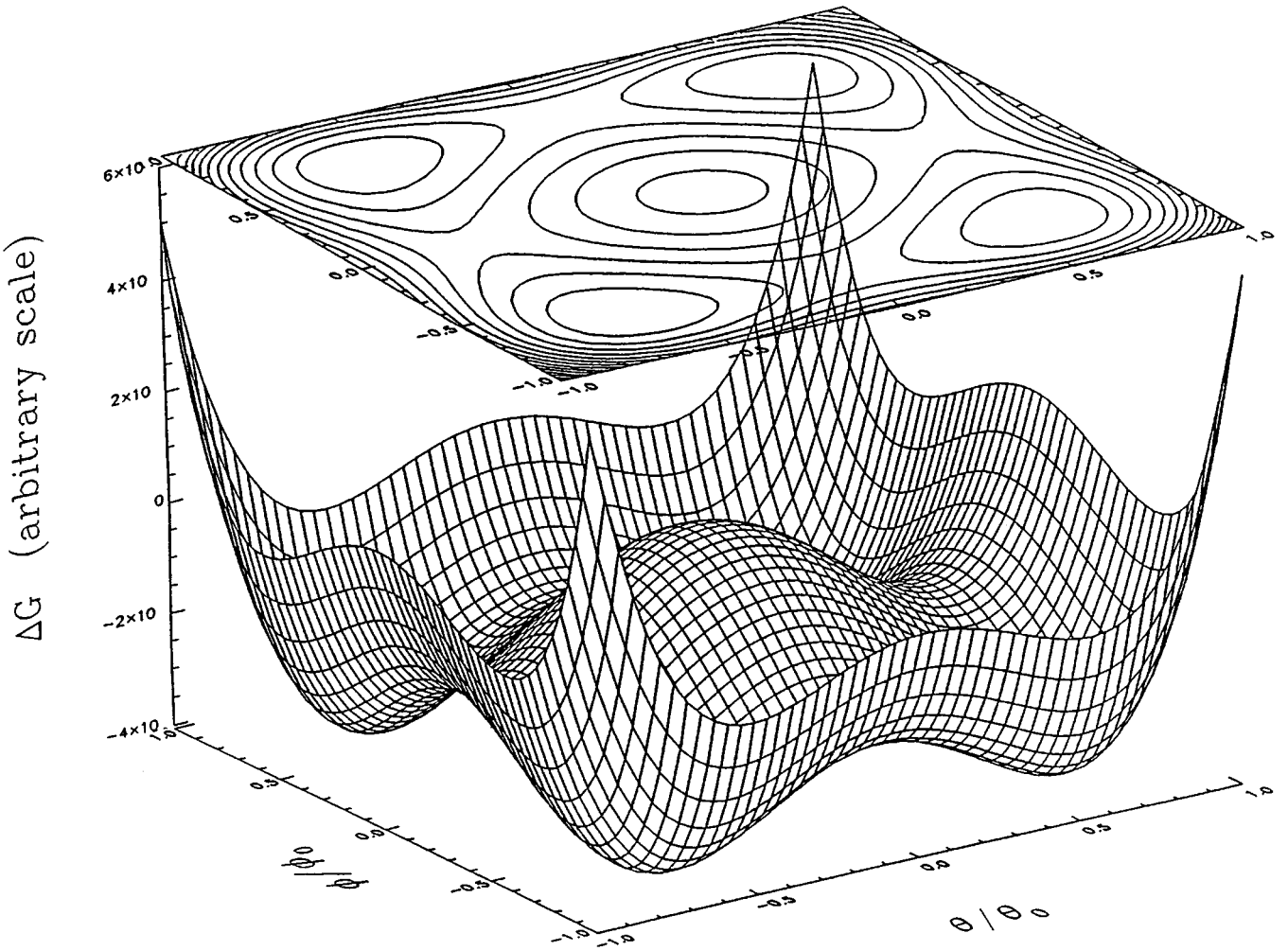

FIG. 11. Free energy of the perovskite structure as a function of normalized tilts θ/θ_0 and ϕ/ϕ_0 plotted in a 3-D space. The contours of the free energy are projected on the plane shown.

also clearly observed that the linear thermal expansions and linear compressibilities show significant anisotropy: $\alpha_a > \alpha_c > \alpha_b$ and $\beta_a > \beta_c > \beta_b$ (Fig. 13). This is directly related to the structural response of the $NaMgF_3$ perovskite to the changes of pressure and temperature. We have demonstrated that the dominant compression mechanism under hydrostatic pressure is the compression of the octahedral Mg–F bond length and that the dominant thermal expansion mechanism is the diminishing of the octahedral tilting angles (21, 22). The tilt-induced volume change contributes about 80% to the overall volumetric thermal expansion of the orthorhombic $NaMgF_3$ perovskite, whereas the expansion of the Mg–F bond contributes only about 20%. For the overall volumetric compression in the orthorhombic $NaMgF_3$ perovskite, the contributions are reversed: the tilt-induced volume change contributes only about 20% whereas the compression of the Mg–F bond contributes about 80% (11, 20–22).

D. Secondary Phase

As described in the previous section, the kink in the phase boundary between orthorhombic *Pbnm* and tetragonal *P*4/*mbm* at about $X = 15\%$ (Fig. 8) may be associated with the existence of a secondary phase. Based on the fact that the extra diffraction peaks are all associated with in-phase tilting ϕ_z^+ of the octahedra, this secondary phase is thus identified to be the tetragonal *P*4/*mbm* structure (3–7). Shown in Fig. 14 are three detailed plots of diffraction patterns from $2\theta = 16^\circ$ to $2\theta = 20^\circ$, which are for the pure *Pbnm* phase of $(K_{0.05}Na_{0.95})MgF_3$ (bottom), the pure *P*4/*mbm* phase of $(K_{0.35}Na_{0.65})MgF_3$ (top), and the mixture

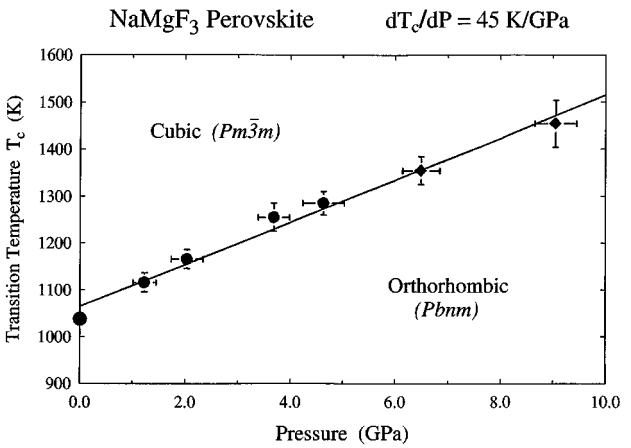

FIG. 12. Transition temperature for the direct orthorhombic–cubic phase transition of the end-member $NaMgF_3$ perovskite as a function of pressure. Linear regression of the data shows a positive slope of $dT_c/dP = 45$ K/GPa.

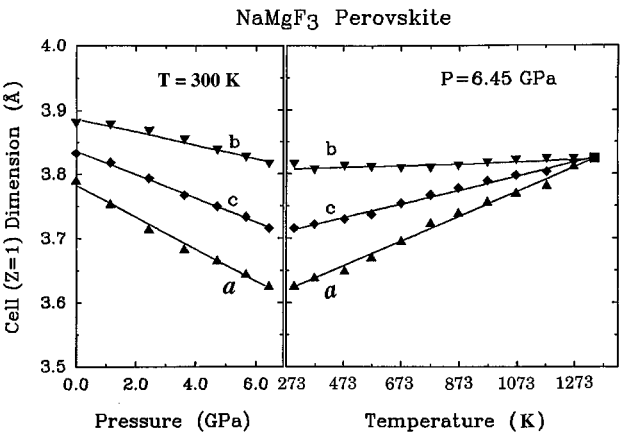

FIG. 13. Unit cell parameters (reduced to a pseudocubic $Z = 1$ prototype cell) of the end-member $NaMgF_3$ perovskite as a function of pressure and temperature. The unit cell dimensions decrease and diverge with increasing pressure and increase and converge with increasing temperature.

phase of $(K_{0.15}Na_{0.85})MgF_3$ (middle). Evidently, there are extra peaks between the $\{120, 210\}_{orth}$, $\{022, 202\}_{orth}$, and $\{122, 212\}_{orth}$ doublets of the *Pbnm* phase of $(K_{0.15}Na_{0.85})MgF_3$ perovskite. These extra peaks can be readily identified as the $(210)_{tetra}$, $(201)_{tetra}$, and $(211)_{tetra}$ peaks of the *P*4/*mbm* phase of $(K_{0.15}Na_{0.85})MgF_3$ perovskite, respectively, as indicated by the arrows in the diagram (middle plot).

This determination is supported by the results of whole-pattern Rietveld refinement of the diffraction spectrum. The structure refinement indicates that the diffraction spectrum can be best fitted in peak position, peak width, and peak intensity for the whole pattern when the tetragonal *P*4/*mbm* is introduced as the second phase. Listed in Table 1 is the structural refinement result for the $(K_{0.15}Na_{0.85})MgF_3$ perovskite. The refinement procedure was started with a single phase of *Pbnm* to refine lattice constants and structural parameters, which resulted in a significant refinement error. The intensity residual R_p, agreement index R_{wp}, and goodness of fit χ^2 (defined in GSAS (10)) all improved significantly when the secondary *P*4/*mbm* phase was introduced into the refinement. The thermal vibrations were refined using isotropic model U_{iso}, and the same elements were bundled together for both phases to better constrain the refinement result. The phase fraction was then refined to be 54.6% for the orthorhombic *Pbnm* phase and 45.4% for the tetragonal *P*4/*mbm* phase of $(K_{0.15}Na_{0.85})MgF_3$ perovskite.

The phase fractions for all $(K_xNa_{1-x})MgF_3$ perovskites have been refined for $x = 0.05$–0.35 and the results are plotted in a bar diagram (Fig. 15). It is found that there is a maximum of about 45.4% phase fraction of the secondary tetragonal *P*4/*mbm* phase at the 15% K^+ concentration, $(K_{0.15}Na_{0.85})MgF_3$, which is well correlated to the observed kink at the phase boundary between orthorhombic and tetragonal. This may be understood from the topological point of view that about 12.5% of large K^+ cations are required to alternately fill the dodecahedral sites in three-dimensional space to give $\sim$50% of the second phase existing in the $(K_xNa_{1-x})MgF_3$ perovskite structure. In a sense, the mixture of the orthorhombic *Pbnm* phase and the tetragonal *P*4/*mbm* phase can be comprehended as co-existing phases within the crystal structure. Further studies using X-ray precession photographs of single-crystal-line $(K_{0.15}Na_{0.85})MgF_3$ and TEM diffraction patterns of polycrystalline $(K_{0.15}Na_{0.85})MgF_3$ show strong diffuse scattering along with Bragg diffractions. This may be attributed to the existence of the local soft phonon mode within the perovskite structure and/or the static order between K and Na. The observation of diffuse scattering provides a complementary explanation for the existence of the secondary tetragonal phase intergrowth with the main orthorhombic phase. The following decrease of the phase fraction in the 20–25% K^+ concentration range may be understood as the result of formation of the two-dimensional layer of the

FIG. 14. Detailed plots of diffraction patterns for the pure *Pbnm* phase of $(K_{0.05}Na_{0.95})MgF_3$ (bottom), the pure *P*4/*mbm* phase of $(K_{0.35}Na_{0.65})MgF_3$ (top), and the mixture phase of $(K_{0.15}Na_{0.85})MgF_3$ (middle). The diagnostic superlattice peaks $\{121, 103, 211\}_{orth}$ triplet and $(113)_{orth}$ singlet clearly disappeared in the tetragonal phase. For the $(K_{0.15}Na_{0.85})MgF_3$ perovskite (middle), extra peaks evidently exist between the $\{120, 210\}_{orth}$, $\{022, 202\}_{orth}$, and $\{122, 212\}_{orth}$ doublets of the orthorhombic *Pbnm* phase. These extra peaks are identified as the $(210)_{tetra}$, $(201)_{tetra}$, and $(211)_{tetra}$ peaks of the tetragonal *P*4/*mbm* phase associated with the in-phase tilting ϕ_z^+.

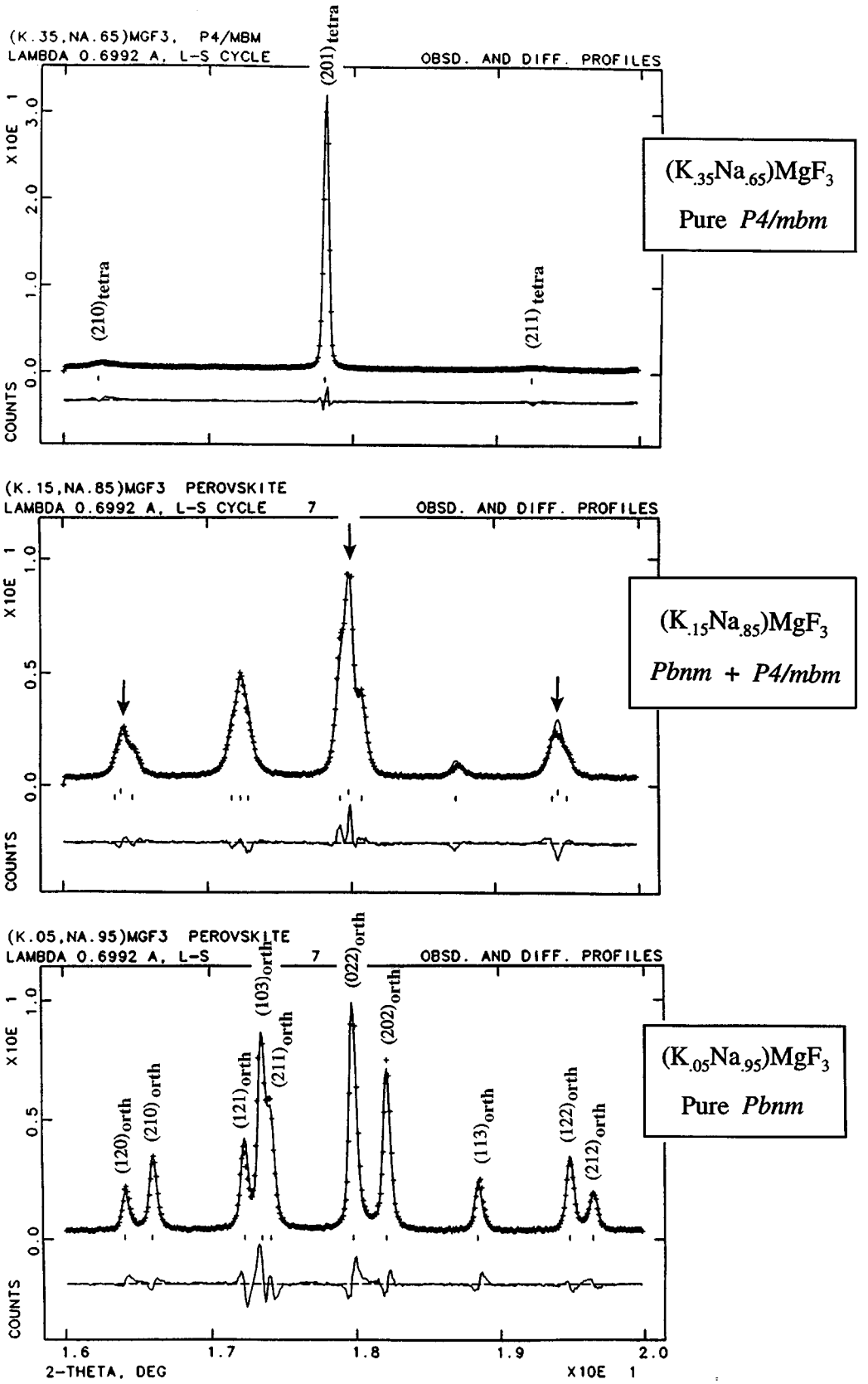
(K.35,NA.65)MGF3, P4/MBM
LAMBDA 0.6992 A, L-S CYCLE
OBSD. AND DIFF. PROFILES
(201) tetra
(210)tetra
(211) tetra
X10E 1
3.0
2.0
1.0
0.0
COUNTS
(K.35,Na.65)MgF3
Pure P4/mbm
(K.15,NA.85)MGF3 PEROVSKITE
LAMBDA 0.6992 A, L-S CYCLE 7
OBSD. AND DIFF. PROFILES
X10E 1
1.0
0.5
0.0
COUNTS
(K.15,Na.85)MgF3
Pbnm + P4/mbm
(K.05,NA.95)MGF3 PEROVSKITE
LAMBDA 0.6992 A, L-S 7
OBSD. AND DIFF. PROFILES
(120)orth
(210) orth
(121)orth
(103)orth
(211)orth
(022)orth
(202)orth
(113)orth
(122)orth
(212)orth
X10E 1
1.0
0.5
0.0
COUNTS
1.6
1.7
1.8
1.9
2.0
2-THETA, DEG
X10E 1
(K.05,Na.95)MgF3
Pure Pbnm

TABLE 1
Structural Refinement of $(K_{0.15}Na_{0.85})MgF_3$ Perovskite

	Orthorhombic *Pbnm*				Tetragonal *P*4/*mbm*			
	a (Å)	*b* (Å)		*c* (Å)	*a* (Å)		*c* (Å)	
	5.4356(6)	5.5020(6)		7.7427(9)	5.4730(8)		3.8727(5)	
	x	*y*	*z*	$100U_{iso}$ (Å^2)	*x*	*y*	*z*	$100U_{iso}$ (Å^2)
$K_{0.15}$	1.042(3)	−0.029(3)	$\frac{1}{4}$	5.9(7)	0	$\frac{1}{2}$	$\frac{1}{2}$	5.9(7)
$Na_{0.85}$	0.988(1)	0.035(1)	$\frac{1}{4}$	2.8(2)	0	$\frac{1}{2}$	$\frac{1}{2}$	2.8(2)
Mg	0	$\frac{1}{2}$	0	2.4(1)	0	0	0	2.4(1)
F(1)	0.076(1)	0.478(1)	$\frac{1}{4}$	4.4(1)	0	0	$\frac{1}{2}$	4.4(1)
F(2)	0.707(1)	0.290(1)	0.044(1)	4.8(1)	0.297(1)	0.203(1)	0	4.8(1)
Phase fraction			0.546(9)			0.454(9)		

Note: $R_p = 0.058$, $R_{wp} = 0.078$, and $\chi^2 = 3.243$ for both structural refinements.

tetragonal phase, which will thus reduce its overall phase fraction in the three-dimensional space.

At K^+ concentrations above 35%, all K^+ and Na^+ cations are located at the ideal position of $(0, \frac{1}{2}, \frac{1}{2})_{tetra}$. All F(1) anions are back at the ideal position of $(0, 0, \frac{1}{2})_{tetra}$ and the *z* component of the F(2) anions also shows no displacement from the $(z = 0)_{tetra}$ position. Thus, the antiphase tilts ϕ_x^- and ϕ_y^- completely disappear, leaving only the in-phase tilt ϕ_z^+. The phase is therefore identified as the pure tetragonal *P*4/*mbm* phase. The tetragonal tilting system $(0, 0, \phi_z^+)$ is written as (0, 0, *c*) in Glazer's notation (3, 4). We have also refined the unit cell dimensions, octahedral tilting, and octahedral bond length of the secondary tetragonal phase for the 5–35% K^+ concentration range, and the results are shown in Fig. 16. It is observed that the increase of unit cell dimensions of the secondary tetragonal *P*4/*mbm* phase at higher K^+ concentrations is accompanied with a significant decrease of the octahedral tiltings, the octahedral bond length is nearly constant.

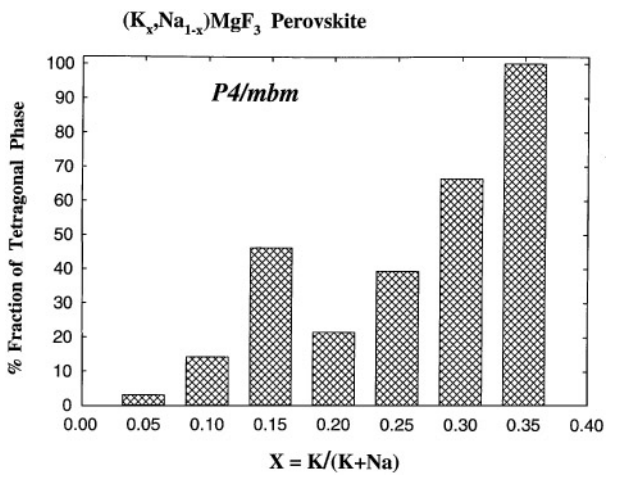

FIG. 15. Phase fraction of the secondary tetragonal *P*4/*mbm* phase (relative to the primary orthorhombic *Pbnm* phase) refined from the diffraction spectra of $(K_xNa_{1-x})MgF_3$ perovskites in the $X = 0.05$–0.35 range.

DISCUSSION AND CONCLUSION

To describe the structural distortion of the ABO_3 perovskites, Goldschmidt introduced a tolerance factor, $t = (R_A + R_O)/\sqrt{2}(R_B + R_O)$, to define the effect of ionic radii (25). For a fixed *B* cation, a smaller size of the 12-coordinated *A* cation will result in a decrease of the tolerance factor and, thus, significant distortion in the crystal structure of perovskite. The small Na^+ cation at the *A* site cannot fill the dodecahedral cavity, and the MgF_6 octahedral framework of the end-member $NaMgF_3$ perovskite collapses to a distorted structure, demonstrated by tilting and rotation of the octahedra. On the other hand, the large K^+ cation can fill the dodecahedral cavity and the end-member $KMgF_3$ perovskite is thus in the cubic phase. As more large K^+ cations are introduced into the crystal structure of the $(K_xNa_{1-x})MgF_3$ perovskites, the tilting angles of the MgF_6 octahedral framework are pushed back to be straight and, at the same time, the octahedral Mg–F bond lengths are compelled to be shorter. Such a process may occur locally around the K^+ cations at low K concentrations of $X \leq 25\%$, as suggested by the diffuse scattering. The gradual decrease of the orthorhombic distortion of the perovskite structure is thus accompanied with the emergence of the secondary tetragonal phase. For the $X = 30$–40% range, the accelerated decreasing in octahedral tilts associated with the rapid reduction of the octahedral bond length results in a transformation to the pure tetragonal phase at X_{c1}(orth–tetra), and, eventually, to the cubic

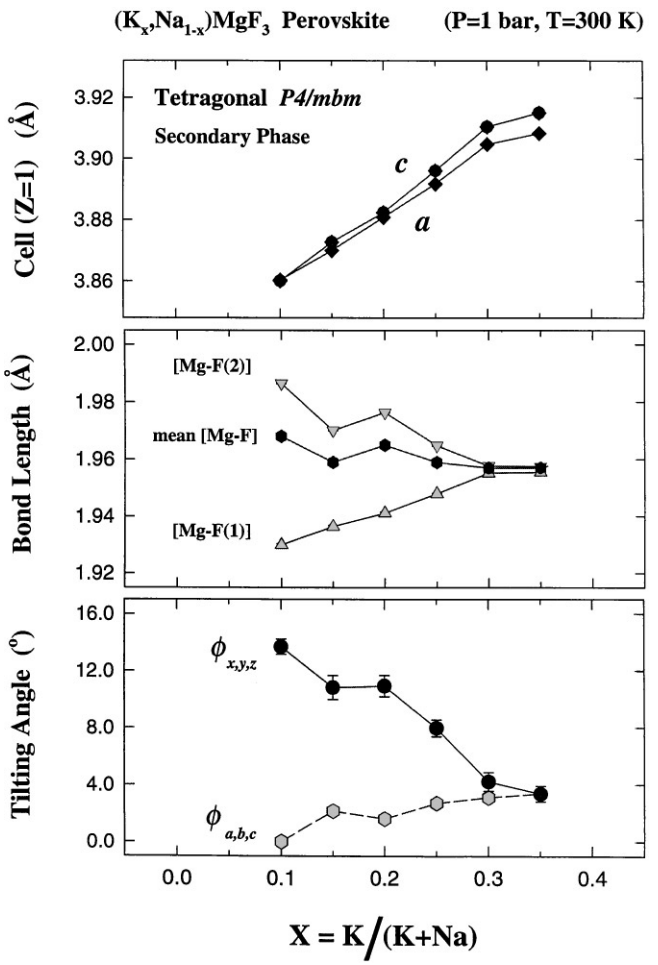

FIG. 16. Unit cell parameters (reduced to a pseudocubic $Z = 1$ prototype cell), octahedral bond length, and octahedral tilting angle of the secondary tetragonal *P*4/*mbm* phase plotted as a function of the K^+ concentration for $(K_xNa_{1-x})MgF_3$ perovskite. The unit cell dimensions increase, the tilting angle decreases, and the mean bond length does not change significantly as more large K^+ cations participate in the perovskite structure.

phases at X_{c2}(tetra–cubic). A similar process is also observed as the temperature approaches the transition temperature T_c, where the effective tolerance factor approaches $t = 1$. The distortion of the (K,Na)MgF_3 perovskite structure can also be modified either by replacing the Mg^{2+} cations with cations of different radii, such as Ca^{2+}, or by replacing F^- with anions of different radii, such as Cl^- (26–28). We recognize that the tolerance factor does point out the important relationship between ionic radii and structure distortion of perovskites, although it cannot define individual space groups as the tilting system does. Still, it can be used as a composition guide for the synthesis-related crystal chemistry.

The present paper describes the structural distortion of perovskite from the point of view of octahedral tilts and it is based on the assumption of regular octahedra throughout the perovskite structure. The octahedral Mg–F bond lengths are obtained from refinement of the positional parameters *x*, *y*, *z* of the Mg and F atoms. The experimental results indicate that the assumption of regular octahedra is valid for the *P*–*T*–*X* range investigated. The octahedral tiltings can be readily derived from atomic displacements *u*, *v*, *w* (which are defined as the atomic shifts away from their ideal positions in the prototype cubic structure) (12):

$$\begin{aligned}\theta &= \tan^{-1}(4\times\sqrt{u_{F(1)}^2 + v_{F(1)}^2}/c)\\ &= \tan^{-1}(4\times\sqrt{2}\times w_{F(2)}/\sqrt{a^2+b^2})\\ \varphi &= \tan^{-1}(4\times\sqrt{u_{F(2)}^2 + v_{F(2)}^2}/\sqrt{a^2+b^2}).\end{aligned} \quad [1]$$

The unit cell dimensions and volume are related to the octahedral tilting and bond length through the relationships (1, 2, 11, 20)

$$\begin{aligned}a &= 2\sqrt{2}[\text{Mg–F}]\cos\theta\cos\varphi,\\ b &= 2\sqrt{2}[\text{Mg–F}]\cos\varphi,\\ c &= 4[\text{Mg–F}]\cos\theta,\end{aligned}$$

and

$$\begin{aligned}V &= 32[\text{Mg–F}]^3\cos^2\theta\cos^2\varphi\\ &= 32[\text{Mg–F}]^3\cos^2\Phi.\end{aligned} \quad [2]$$

The expansion and compression of the perovskite structure due to the variation of pressure, temperature, and composition can be modeled in terms of the change in octahedral bond lengths and octahedral tilts. We proposed a structural model for thermal expansion and compression of the perovskite structure in which the overall volumetric change of the distorted perovskite structure can be decoupled into two constituent components: one is the volume change of the octahedra, i.e., the octahedral bond length change; and the other is the volume change due to the octahedral tilting (21, 22):

$$\alpha_V = \alpha_{V_o} + \alpha_{V_\Phi} = \frac{3}{[\text{Mg–F}]}\left(\frac{\partial[\text{Mg–F}]}{\partial T}\right) + \frac{2}{\cos\Phi}\left(\frac{\partial\cos\Phi}{\partial T}\right) \quad [3]$$

and

$$\beta_V = \beta_{V_o} + \beta_{V_\Phi} = -\frac{3}{[\text{Mg–F}]}\left(\frac{\partial[\text{Mg–F}]}{\partial P}\right) - \frac{2}{\cos\Phi}\left(\frac{\partial\cos\Phi}{\partial P}\right).$$

This structural model follows the analysis of Megaw (23) and Hazen and Finger (24). The overall volumetric change

of the distorted perovskite structure due to the composition change can also be described using the same analogy.

In summary, we have demonstrated that the volumetric change of the perovskite structure can be decoupled into two constituent parts: the expansion/compression of the octahedral bond length Mg–F and the expansion/compression due to the MgF_6 octahedral tilting Φ. The experimental data show that thermal expansion of the perovskite is mostly accommodated by the octahedral tilting, whereas the dominant compression mechanism for the perovskite is octahedral bond compression. It is demonstrated that the drastic shrinkage of the Mg–F bond length is always accompanied by the rapid diminishing of the MgF_6 octahedral tilting as observed around phase transition T_c and X_c. With change of pressure, temperature, and K^+ incorporation, the $(K,Na)MgF_3$ perovskite shows reversible structural phase transitions from orthorhombic *Pbnm* to tetragonal *P*4/*mbm* to cubic *Pm*3*m*. The observed direct orthorhombic–cubic phase transition for the end-member $NaMgF_3$ preovskite is a unique and unusual phase transition. It is driven by strong coupling between the order parameters—octahedral tiltings θ and φ—via significant anharmonic thermal vibrations. Many critical phenomena associated with the soft phonon processes are observed as the structural phase transition occurs. The experimental results show that the transition temperatures increase with increasing pressure and decrease with increasing K^+ concentration.

ACKNOWLEDGMENT

We thank D. J. Weidner, J. B. Parise, and D. E. Cox for their support in the experiments. The X7A/PSD/NSLS and X17B/SAM-85/NSLS projects related to this study were supported by an NSF grant to the Center for High Pressure Research (CHiPR) (Grant EAR-8920239). This work was supported by the U.S. Department of Energy under Contract W-7405-ENG-36 with the University of California, the Los Alamos Branch of the Institute of Geophysics and Planetary Physics, and Los Alamos Laboratory-Directed Research and Development funding.

REFERENCES

1. M. O'Keeffe and B. G. Hyde, *Acta Crystallogr., Sect. B* **33,** 3802 (1977).
2. M. O'Keeffe, B. G. Hyde, and J. O. Bovin, *Phys. Chem. Miner.* **4,** 299 (1979).
3. A. M. Glazer, *Acta Crystallogr., Sect. B* **28,** 3384 (1972).
4. A. M. Glazer, *Acta Crystallogr., Sect. A* **31,** 756 (1975).
5. K. S. Aleksandrov, *Ferroelectrics* **16,** 801 (1976).
6. K. S. Aleksandrov, *Ferroelectrics* **20,** 61 (1978).
7. K. S. Aleksandrov and S. V. Misyul, *Sov. Phys. Crystallogr.* **26,** 612 (1981).
8. D. E. Cox, B. H. Toby, and M. M. Eddy, *Aust. J. Phys.* **41,** 117 (1988).
9. H. M. Rietveld, *J. Appl. Crystallogr.* **2,** 65 (1969).
10. A. C. Larson and R. B. VonDreele, LAUR 86-748, Los Alamos National Laboratory, 1988.
11. Y. Zhao, D. J. Weidner, J. B. Praise, and D. E. Cox, *Phys. Earth Plant. Int.* **76,** 1 (1993).
12. Y. Zhao, D. J. Weidner, J. B. Praise, and D. E. Cox, *Phys. Earth Plant. Int.* **76,** 17 (1993).
13. L. D. Landau and E. M. Lifshitz, "Statistical Physics." Pergamon, Oxford, 1969.
14. A. M. Glazer and H. D. Megaw, *Philos. Mag.* **25,** 1119 (1972).
15. R. A. Cowley, *Phys. Rev. B* **13,** 4877 (1976).
16. J. C. Toledano and P. Toledano, *Phys. Rev. B* **21,** 1139 (1980).
17. V. K. Wadhawan, *Phase Transitions* **3,** 3 (1982).
18. G. A. Samara, T. Sakudo, and K. Yoshimitsu, *Phys. Rev. Lett.* **35,** 1767 (1975).
19. D. J. Weidner and SAM-85 team, *High-Pressure Res.* **8,** 617 (1992).
20. Y. Zhao, D. J. Weidner, and SAM-85 team. *J. Geophys. Res.* **99,** 2871 (1994).
21. Y. Zhao and D. J. Weidner, *Phys. Chem. Miner.* **20,** 419 (1991).
22. Y. Zhao, J. B. Parise, Y. Wang, K. Kusaba, M. T. Vaughan, D. J. Weidner, T. Kikegawa, J. Chen, and O. Shimomura, *Am. Miner.* **79,** 615 (1994).
23. H. D. Megaw, *Mater. Res. Bull.* **6,** 1007 (1971).
24. R. M. Hazen and L. W. Finger, "Comparative Crystal Chemistry." Wiley, New York, 1982.
25. V. W. Goldschmidt, *J. Math. Naturvid. Klass.* **2,** 97 (1926).
26. A. Ratuszna, Ph. Daniel, and M. Rousseau, *Phase Transitions* **54,** 43 (1995).
27. P. C. Burns, F. C. Hawthorne, A. M. Hofmeister, and S. L. Moret, *Phys. Chem. Miner.* **23,** 141 (1996).
28. J. W. Flocken, W. N. Mei, R. A. Guenther, J. R. Hardy, P. J. Edwardson, and L. L. Boyer, *Phase Transitions* **20,** 113 (1990).
29. L. Topor, A. Navrosky, Y. Zhao, and D. J. Weidner, *J. Solid State Chem.* **132,** 131 (1997).